



Optics Letters

Precise 3D particle localization over large axial ranges using secondary astigmatism

YONGZHUANG ZHOU AND GUILLEM CARLES*

School of Physics and Astronomy, University of Glasgow, Glasgow G12 8QQ, UK

*Corresponding author: Guillem.CarlesSantacana@glasgow.ac.uk

Received 20 January 2020; revised 28 February 2020; accepted 28 February 2020; posted 28 February 2020 (Doc. ID 388695); published 15 April 2020

We propose an analytical pupil phase function employing cropped secondary astigmatism for extended-depth nanoscale 3D-localization microscopy. The function provides high localization precision in all three dimensions, which can be maintained over extended axial ranges, customizable up to two orders of magnitude relative to the conventional, diffraction-limited imaging. This enables, for example, capturing nanoscale dynamics within a whole cell. The flexibility and simplicity in the implementation of the proposed phase function make its adoption in localization-based microscopy attractive. We demonstrate and validate its application to real-time imaging of 3D fluid flow over a depth of 40 μm with a numerical aperture of 0.8.

Published by The Optical Society under the terms of the [Creative Commons Attribution 4.0 License](https://creativecommons.org/licenses/by/4.0/). Further distribution of this work must maintain attribution to the author(s) and the published article's title, journal citation, and DOI.

<https://doi.org/10.1364/OL.388695>

Point emitters are used widely in science and engineering as tracers of three-dimensional velocity fields, indicators of mechanical forces, or labels of biomedical structures. Precise localization of microscopic or nanoscopic point emitters has aroused broad interest over the past decade, particularly because of its applications in life sciences to super-resolution microscopy [1–3] and single-molecule tracking experiments [4–7], which have revolutionized our ability to resolve subcellular structures beyond the diffraction limit and to study fundamental biological dynamics such as folding and unfolding of proteins, protein–DNA interaction, and dynamic processes on cell membranes [8]. Moreover, it has found its application on a larger scale in blood-flow characterization [9–11], traction-force microscopy [12,13], and microfluidic research [14] including lab-on-chip experiments [15,16].

Several methods exist to perform localization of point emitters in all three dimensions [17]. The use of an astigmatic point-spread function (PSF) is perhaps the simplest and most widely used method, but other more elaborated techniques have been developed, such as the self-bending, corkscrew, Airy-beam, parallax, double-helix and tetrapod PSFs [18–27]. Among them, the double-helix PSF has proved successful in a range

of low-photon-count applications [24,25]. It is an example of the so-called engineered PSF methods, which involve the use of phase modulation at the pupil of the microscope with the aim of optimizing the PSF against some criteria, in this case to provide high 3D localization precision. The double-helix PSF has the additional ability to provide some extension of the axial range over which precise 3D localization can be achieved; however, an axial range in excess of 3 μm has not been reported on high numerical aperture (NA) systems. This precludes the application of such approaches to whole-cell imaging or imaging of larger length scale structures of interest. Airy-beam PSFs provide great extension of the depth range [21,22] and have the additional benefit of the imaging capability being retained (i.e., the modulation-transfer function transmits all frequencies up to the optical cutoff), although this is not a requirement for particle localization, and the precision is sub-optimal. The search for an engineered PSF that maintains optimal localization precision over a defined axial range was rigorously formulated by Shechtman *et al.* [26,27] who synthesized a family of “tetrapod” PSFs, that carry the most information for localizing the emitter in both axial and transverse directions. The phase modulation was numerically defined using the first 55 Zernike polynomials, and the coefficients were optimized against the Cramer–Rao lower bound (CRLB) on 3D localization precision over the desired axial range. Such PSFs were reported to yield 20 μm axial range on a 1.4 NA system, which is a magnitude more than other existing approaches. However, the optimization process needs to be repeated for each particular optical system and configuration, e.g., when changing the operable axial range, and it is prone to fall into local minima in a high-dimensional space (unless time-consuming global search is employed). Indeed, a range of differing tetrapod masks have been reported [26,27]. On the other hand, the ability to formulate the phase modulation with an analytical expression is of high interest. In fact, considerable effort has been put into finding analytical expressions for other PSFs such as the double-helix PSF [28].

In this Letter, we propose a simple and analytical phase function, termed the cropped oblique secondary astigmatism (COSA), that produces a PSF that provides equivalent axial range and localization precision to the tetrapod PSF. It thus provides a depth range larger than other existing techniques. The shape of the COSA mask is analytical and requires no optimization, so it can be readily implemented in any microscopy system.

The operable depth range is easily adjusted through a single parameter, i.e., the COSA coefficient α , which sets the strength of the mask. It balances the compromise between localization precision and the extent of the operable axial range. We formulate and analyze the localization performance of the proposed COSA phase mask and report its experimental demonstration, implemented using a deformable mirror on a microscope setup. We also report experiments on particle tracking velocimetry in a microfluidic flow using the proposed COSA PSF, showing its suitability for 3D particle localization applications that require extended axial ranges.

The PSF of a microscope system equipped with a phase mask in its pupil plane takes the form (in scalar diffraction theory)

$$\text{PSF} \propto \left| \mathcal{F} \left\{ A(\rho, \phi) e^{2\pi i(\psi(\rho, \phi) + D(\rho, z))} \right\} \right|^2, \quad (1)$$

where $\mathcal{F}\{\cdot\}$ stands for Fourier transform, (ρ, ϕ) are the pupil coordinates in normalized polar form ($\rho = r/R$, where r is the radial coordinate and R is the radius of the aperture), $A(\rho, \phi)$ is the pupil amplitude function, $\psi(\rho, \phi)$ is the modulation imparted by the phase mask, $D(\rho, z) = z\lambda^{-1}\sqrt{n^2 + \text{NA}^2\rho^2}$ is the defocus phase that occurs when the emitter is displaced by z from the focal plane, n is the refractive index of the medium between the emitter and the objective, and λ is the wavelength of light. By finding an appropriate phase modulation ψ , the PSF is engineered to a particular shape in three dimensions. The goal is therefore to design the phase modulation ψ such that the precision in determining the (x, y, z) location of the emitter is optimal, using the 2D slice of the 3D PSF.

As mentioned above, tetrapod PSFs are defined numerically using a series of Zernike polynomials that needs to be optimized against a CRLB-based metric. Exploring the optimization space, we observe that the process tends to cluster around two prominent Zernike polynomials, namely, oblique astigmatism and oblique secondary astigmatism with a particular relative weight. Following this suggestive finding, we define the COSA phase mask as

$$\psi(\rho, \phi) = \alpha(\rho^4 - \rho^2) \sin(2\phi), \quad (2)$$

where α is the mask strength. The mask can also be expressed using the Zernike polynomials $Z_n^m(\rho, \phi)$ as

$$\psi(\rho, \phi)/\alpha = Z_4^{-2}(\rho, \phi)/\sqrt{160} - Z_2^{-2}(\rho, \phi)/\sqrt{96}, \quad (3)$$

$$= Z_4^{-2}(\sqrt{3/4}\rho, \phi)/\sqrt{405/8}, \quad (4)$$

and the latter expression corresponds to a scaled and cropped version of the oblique secondary astigmatism term, hence the name of the proposed phase mask.

The form of the COSA mask and associated PSFs are shown in Fig. 1. The strength of the mask is defined by the parameter α : a higher value provides a larger depth range of the system at the expense of a reduced achievable localization precision.

The maximum localization precision, evaluated by the CRLB limit, for the COSA PSF is shown in Fig. 2, compared with the commonly used astigmatic PSF, the double-helix PSF, and two optimization instances of tetrapod PSFs. (We optimized a range of tetrapod PSFs, and for the selected configuration, they clustered around the two shown instances, as they correspond to local minima in the optimization space.) The plots show the axial localization precision (continuous lines, in the

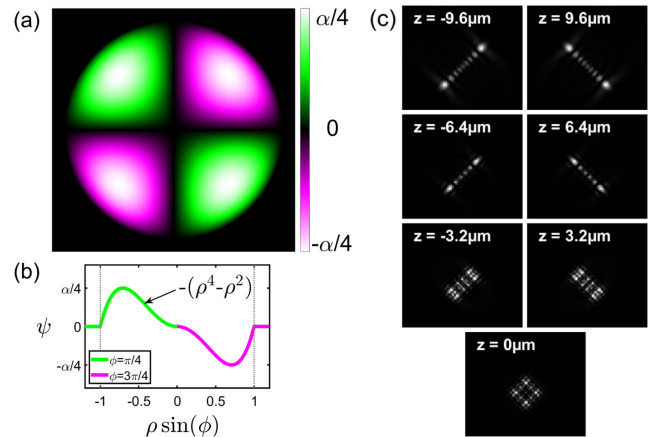


Fig. 1. (a) COSA phase mask and (b) phase profiles in the diagonal ($\sin \phi = 1$) and anti-diagonal ($\sin \phi = -1$) directions. (c) Simulated PSFs at several axial positions for $\alpha = 4.2$ ($\text{NA} = 0.8$, $\lambda = 620 \text{ nm}$). See Visualization 1 for a 3D representation of the COSA PSF.

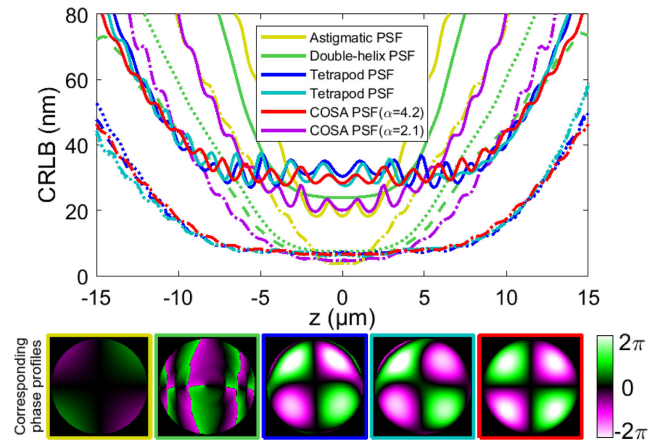


Fig. 2. Calculated CRLB limit for emitter localization, assuming 4000 collected photons, background signal of 10 photons per pixel, and water immersion. Curves are shown for an astigmatic PSF, double-helix PSF, two optimization instances of tetrapod PSFs (optimized over $\pm 10 \mu\text{m}$), and the COSA mask for two different strengths, for the axial direction (continuous lines, for z direction) and transverse directions (discontinuous and dotted lines, for x and y directions, respectively, which overlap where they coincide).

z direction) and the transverse localization precision (discontinuous and dotted lines, in the x and y directions, respectively). Considering the large depth ranges contemplated here, the COSA mask has a performance comparable to the tetrapod PSFs and outperforms the other PSFs. For smaller depth ranges, a weaker COSA mask also yields better performance than the double-helix PSF in terms of both depth range and precision.

Because the COSA PSF has a single parameter (the mask strength, α), its optimization for a particular configuration is straightforward. We calculated the optimum strength as a function of the desired operational depth range and for different NAs. The results show a linear relation, as is appreciated in Fig. 3. We observed virtually no dependence on the number of photons per emitter or on the background light, and the dependence on the desired depth range and NA may be heuristically modeled as

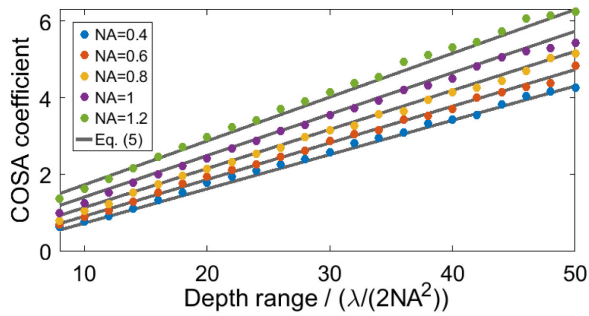


Fig. 3. Optimized COSA coefficient as a function of the desired full depth range ($\lambda = 620$ nm). Depth is normalized by $\lambda/(2NA^2)$ to enable comparison through a range of NAs.

$$\alpha = d \frac{NA^2(C_1 + C_2NA)}{\lambda} + (C_3 + C_4NA^2), \quad (5)$$

where d is the desired full depth range, and constants C_i evaluate to $C_1 = 0.154$, $C_2 = 0.062$, $C_3 = -0.261$, and $C_4 = 0.587$, by least-squares fitting to the data shown in Fig. 3. Equation (5) thus serves as a comprehensive guide to select the COSA mask strength as a function of the desired depth range and the NA of the imaging system. It should be noted that, in order to compare systems with different NAs, the depth range in the plot in Fig. 3 was normalized by $\lambda/(2NA^2)$.

The COSA phase mask and PSF were tested experimentally on a $4f$ system employing a deformable mirror (Iris AO PTT489-5; 255-actuator configuration), as shown in Fig. 4. Each hexagon-shaped actuator mirror can exhibit piston in z and tilts in x and y ; thus, a semi-continuous phase modulation is displayed. Because the phase profile of the COSA mask is relatively smooth, the deviation from the ideal phase due to the segmentation is very small (root-mean-squared error below $\lambda/30$ and peak error below $\lambda/5$ for $\alpha = 4.2$). A 0.8 NA, 40X water immersion objective was used to launch wide-field epillumination and to collect fluorescence light from the sample. The tube lens focal length was 200 mm, and the relay lenses had focal lengths of 125 mm, demagnifying the pupil size to approximately 5 mm at the plane of the deformable mirror (there were about eight segments across the diameter of the pupil in this case; see bottom-left image in Fig. 4). An image was then formed on a sCMOS camera with 2048×2048 pixels.

COSA PSFs were measured by imaging a single sub-diffraction-limit fluorescent bead immobilized in agarose in a fluorinated ethylene propylene (FEP) tube, which was mounted on a motorized translation stage moving in z . The measured PSF stacks are shown in Fig. 5(a) for $\alpha \approx 5.4$ and in Fig. 5(b) for $\alpha \approx 8$, exhibiting an axial range in excess of 20 μm and 32 μm , respectively. The intensity profiles are consistent with the simulation results in Fig. 1 with four bright lobes near the focal plane and two bright lobes aligned to the image diagonal or anti-diagonal directions depending on the sign of the defocus parameter. Different algorithms can be used to localize the emitter in 3D from the shape and location of the PSF within the image. The achieved localization precision will depend on their performance, ultimately approaching the CRLB limit. Maximum-likelihood estimation [26,29] can be used to optimally fit a model of the 3D PSF (which must include any optical aberrations) to the recorded intensity pattern, assuming the noise is Poissonian. To estimate the experimental localization precision, we employed maximum-likelihood estimation to

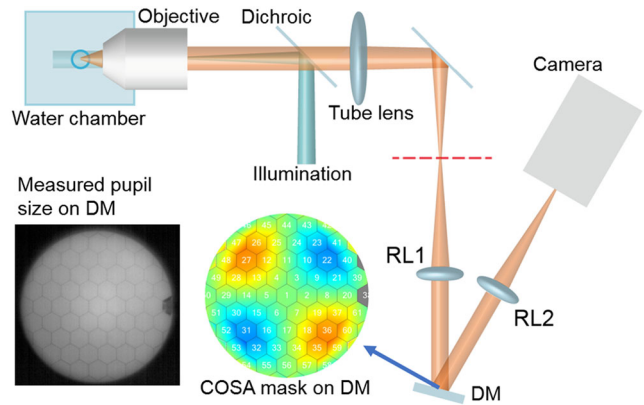


Fig. 4. Experimental setup employing a water immersion objective (Nikon CFI Apo NIR 40X W), a $4f$ system using relay lenses (RL), and a deformable mirror (DM).

perform repeated localizations of a single quantum dot. We obtained a mean localization precision of 24.7 nm transversely and 37.7 nm axially using a COSA mask with $\alpha = 5.4$ within 12 μm axial range near the focus, with approximately 5500 photons per localization and 13 background photons per pixel. For low-photon-count experiments, maximum-likelihood estimation may be required for satisfactory performance, but for higher photon budgets, a simpler algorithm is preferred, and can also be more robust, for example, to unknown system aberrations. For subsequent experiments, we exploited the symmetry of the COSA PSF to determine the depth by finding the relative distance between its main lobes, which although sub-optimal is simpler and computationally faster than maximum-likelihood estimation. The fact that these localization algorithms are based on calibration (a measured stack of PSFs is used) combined with the phase encoding of the COSA mask suppresses the impact of modest optical aberrations, including the effect of the segmentation of the deformable mirror. Also, these algorithms assume PSFs from different emitters are isolated (as is usually the case for applications such as single-molecule tracking and localization). For higher emitter density, the algorithms need to deal with overlapping PSFs. This can be done, for example, by calculating the joint maximum-likelihood of emitter clusters or by using iterative approaches, although the localization precision unavoidably degrades.

We used the COSA PSF to perform particle tracking velocimetry in microfluidics. Water traced with fluorescent particles was pumped through an FEP tube with an inner diameter of about 93 μm . We twisted the tube to form a helix, so that it created a non-rectilinear 3D velocity field, to be imaged. The twisted FEP tube was immersed in the water chamber to match the refractive index and minimize refraction errors. A section of approximately 200 μm in length was imaged, and the flowing fluorescent particles were tracked through their trajectory in the 3D velocity field, exploiting the extended-range and localization capability of the COSA phase mask. A plot of the measured trajectories is shown in Fig. 5(c); see Visualization 2 for the recorded flow in real time and the reconstructed trajectories.

We now discuss the mechanisms that provide the COSA mask with its depth extension and localization capabilities. The shape of the COSA mask has two peaks and two valleys, which effectively divide the pupil into four pseudo-lenslets, in two pairs of opposite optical power and with an effective lower NA.

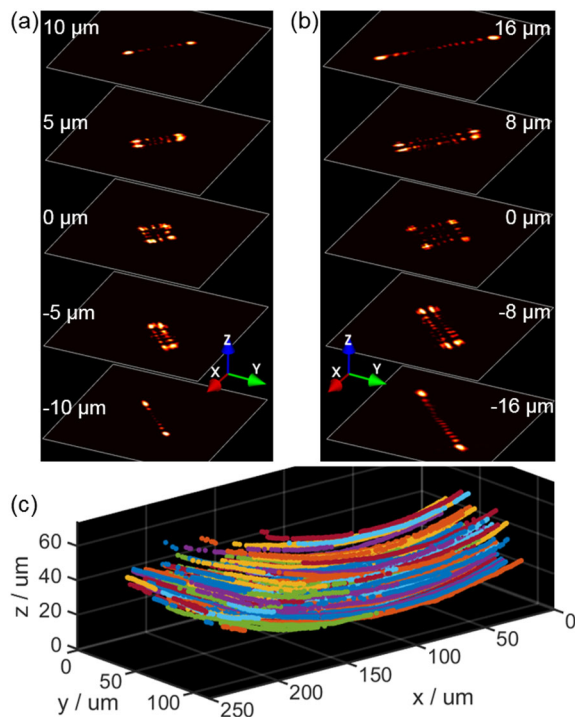


Fig. 5. Measured PSF stacks by imaging a single immobilized sub-diffraction limit fluorescent bead for (a) $\alpha \approx 5.4$ and (b) $\alpha \approx 8$. (c) Tracking of 3D fluid flow traced with fluorescent particles; the trajectories of different tracer particles are color-coded for visibility. See Visualization 2 for the recorded flow in real time, together with the reconstructed 3D trajectories.

Each of these lenslets shifts its associated focal point laterally (because they are placed off-axis) and axially (because they have an effective optical power), creating the characteristic diagonal and anti-diagonal lobes in each side of the system's focal plane. The overall depth range is therefore extended due to this axial shift in opposite sides of the system focal plane, and also due to the depth-of-field extension caused by the effective lower NA that can be associated to each lenslet. Additionally, because the lenslets are placed off-axis, the lobes translate laterally with defocus (they separate as the source moves away from the focal plane), providing the z -localization capability of the mask; see Visualization 1. However, even though this separation into four channels is useful to understand the operation of the COSA mask, they are not completely independent, and light from the entire pupil interferes to form the 3D PSE, which is particularly noticeable near the focal plane where the square-shaped diffraction pattern is formed. That is, the mask should still be understood as an aberration acting over the entire NA. This interference from the use of full NA, increases the compactness of the lobes increasing the lateral localization precision.

In summary, we have proposed a new phase mask for PSF-engineered microscopy that allows to perform localization of point emitters in three dimensions and over an axial range that can be extended up to two orders of magnitude compared with the native depth of field of the objective. The performance of the phase mask, in terms of the achievable localization precision, is superior or comparable to any state-of-the-art alternatives, but has the additional advantage that it can be synthesized through a simple analytical expression. This makes it attractive to be adopted by users in localization-based microscopy, as Eqs. (2)

and (5) can be used to readily implement the phase mask to any given microscopy setup, and no complex optimization is required. We have implemented such phase mask with a deformable mirror, and used it to track particles over a depth range of 40 μm using a 0.8 NA objective, and demonstrated the measurement of microfluidic flow as an example application.

Funding. Leverhulme Trust (ECF-2016-757); Engineering and Physical Sciences Research Council (EP/M028135/1).

Acknowledgment. The authors are grateful to Dr. Jonathan M. Taylor for fruitful discussions.

Disclosures. The authors declare no conflicts of interest.

REFERENCES

1. M. G. L. Gustafsson, *J. Microsc.* **198**, 82 (2000).
2. M. J. Rust, M. Bates, and X. Zhuang, *Nat. Methods* **3**, 793 (2006).
3. E. Betzig, G. H. Patterson, R. Sougrat, O. W. Lindwasser, S. Olenych, J. S. Bonifacino, M. W. Davidson, J. Lippincott-Schwartz, and H. F. Hess, *Science* **313**, 1642 (2006).
4. E. B. Shera, N. K. Seitzinger, L. M. Davis, R. A. Keller, and S. A. Soper, *Chem. Phys. Lett.* **174**, 553 (1990).
5. G. J. Schütz, G. Kada, V. P. Pastushenko, and H. Schindler, *EMBO J.* **19**, 892 (2000).
6. A. D. Douglass and R. D. Vale, *Cell* **121**, 937 (2005).
7. G. Sancataldo, L. Scipioni, T. Ravasenga, L. Lanzano, A. Diaspro, A. Barberis, and M. Duocastella, *Optica* **4**, 367 (2017).
8. H. Shen, L. J. Tauzin, R. Baiyasi, W. Wang, N. Moringo, B. Shuang, and C. F. Landes, *Chem. Rev.* **117**, 7331 (2017).
9. D. R. Larson, W. R. Zipfel, R. M. Williams, S. W. Clark, M. P. Bruchez, F. W. Wise, and W. W. Webb, *Science* **300**, 1434 (2003).
10. Y. Geng, P. Dalhaimer, S. Cai, R. Tsai, M. Tewari, T. Minko, and D. E. Discher, *Nat. Nanotechnol.* **2**, 249 (2007).
11. R. Lima, S. Wada, S. Tanaka, M. Takeda, T. Ishikawa, K.-I. Tsubota, Y. Imai, and T. Yamaguchi, *Biomed. Microdevices* **10**, 153 (2008).
12. W. R. Legant, J. S. Miller, B. L. Blakely, D. M. Cohen, G. M. Genin, and C. S. Chen, *Nat. Methods* **7**, 969 (2010).
13. S. Khetan, M. Guvendiren, W. R. Legant, D. M. Cohen, C. S. Chen, and J. A. Burdick, *Nat. Mater.* **12**, 458 (2013).
14. J. Westerweel, *Meas. Sci. Technol.* **8**, 1379 (1997).
15. A. K. Singh, E. B. Cummings, and D. J. Throckmorton, *Anal. Chem.* **73**, 1057 (2001).
16. R. Lindken, M. Rossi, S. Große, and J. Westerweel, *Lab Chip* **9**, 2551 (2009).
17. Y. Zhou, M. Handley, G. Carles, and A. R. Harvey, *APL Photon.* **4**, 060901 (2019).
18. H. P. Kao and A. S. Verkman, *Biophys. J.* **67**, 1291 (1994).
19. S. Jia, J. C. Vaughan, and X. Zhuang, *Nat. Photonics* **8**, 302 (2014).
20. M. D. Lew, S. F. Lee, M. Badiestostami, and W. E. Moerner, *Opt. Lett.* **36**, 202 (2011).
21. P. Zammit, A. R. Harvey, and G. Carles, *Optica* **1**, 209 (2014).
22. Y. Zhou, P. Zammit, G. Carles, and A. R. Harvey, *Opt. Express* **26**, 7563 (2018).
23. Y. Sun, J. D. McKenna, J. M. Murray, E. M. Ostap, and Y. E. Goldman, *Nano Lett.* **9**, 2676 (2009).
24. S. R. P. Pavani and R. Piestun, *Opt. Express* **16**, 3484 (2008).
25. S. R. P. Pavani, M. A. Thompson, J. S. Biteen, S. J. Lord, N. Liu, R. J. Twieg, R. Piestun, and W. E. Moerner, *Proc. Natl. Acad. Sci. USA* **106**, 2995 (2009).
26. Y. Shechtman, S. J. Sahl, A. S. Backer, and W. E. Moerner, *Phys. Rev. Lett.* **113**, 133902 (2014).
27. Y. Shechtman, L. E. Weiss, A. S. Backer, S. J. Sahl, and W. E. Moerner, *Nano Lett.* **15**, 4194 (2015).
28. G. Grover, K. DeLuca, S. Quirin, J. DeLuca, and R. Piestun, *Opt. Express* **20**, 26681 (2012).
29. A. V. Abraham, S. Ram, J. Chao, E. S. Ward, and R. J. Ober, *Opt. Express* **17**, 23352 (2009).